
Article:
Damian, D., Price, K., Arabagi, S. et al. (2018) In Vivo Tissue Regeneration with Robotic Implants. Science Robotics, 13 (14). eaaq0018.

https://doi.org/10.1126/scirobotics.aaq0018

In Vivo Tissue Regeneration with Robotic Implants

Dana D. Damian[1,2,*], Karl Price[1,*], Slava Arabagi[3], Ignacio Berra[4], Zurab Machaidze[1], Sunil Manjila[5], Shogo Shimada[6], Assunta Fabozzo[7], Gustavo Arnal[1], David Van Story[1], Jeffrey D. Goldsmith[1], Agoston T. Agoston[8], Chunwoo Kim[9], Russell Jennings[1], Peter D. Ngo[1], Michael Manfredi[1], Pierre E. Dupont[1†]

Affiliations:

[1] Boston Children's Hospital, Harvard Medical School, Boston, MA 02115, United States
[2] University of Sheffield, Sheffield, S13JD, United Kingdom
[3] Helbling Precision Engineering, Cambridge, MA 02142, United States
[4] National Pediatric Hospital J.P. Garrahan, Buenos Aires, 01712, Argentina
[5] McLaren Bay Neurosurgery Associates, Bay City, MI 48706, United States
[6] The University of Tokyo Hospital, Tokyo, 1138655, Japan
[7] Hospital of Padua, Padua, 35128, Italy
[8] Brigham and Women's Hospital, Harvard Medical School, Boston, MA 02115, United States
[9] Korea Institute of Science and Technology, Seoul, 02792, Republic of Korea
[*] Co-first authors.
[†] Corresponding author. Email: Pierre.Dupont@childrens.harvard.edu

Abstract:

Robots that reside inside the body to restore or enhance biological function have long been a staple of science fiction. Creating such robotic implants poses challenges both in signaling between the implant and the biological host as well as in implant design. To investigate these challenges, we created a robotic implant to perform in vivo tissue regeneration via mechano-stimulation. The robot is designed to induce lengthening of tubular organs, such as the esophagus and intestines, by computer-controlled application of traction forces. Esophageal testing in swine demonstrates that the applied forces can induce cell proliferation and lengthening of the organ without a reduction in diameter, while the animal is awake, mobile and able to eat normally. Such robots can serve as research tools for studying mechanotransduction-based signaling and can also be employed clinically for conditions such as long-gap esophageal atresia and short bowel syndrome.

One Sentence Summary:

We have created a robotic implant for inducing tissue growth in tubular organs and demonstrated its potential through esophageal lengthening in swine.

Introduction

Robotics has been successfully applied to the restoration of human health as well as to the augmentation of human capabilities. Clinically-approved robots are available for performing minimally invasive surgical procedures (*1*, *2*) and for assisting stroke victims in relearning motor control tasks (*3*, *4*). Robotic prostheses have been designed to replace human limbs (*5*, *6*) while soft and hard exoskeletons are being developed to enhance human strength and endurance (*7*, *8*). These types of robots, however, respond only to conscious motion commands. Also, these robots

either remain outside the human body or enter the body for a short period of time, typically the duration of a medical procedure. In contrast, robotic implants represent an unexplored frontier. Such devices can be implanted in the body for an extended period of time and interact mechanically with tissues to regulate tissue forces or fluid flow rates (*9*) in response to sensed physiological signals as well as external commands.

One intriguing application for robotic implants is mechano-stimulation-modulated tissue regeneration. While in vivo tissue engineering is based on the implantation of a cell-seeded scaffold, an alternate approach is to employ mechanical stimulation of existing tissues to induce their growth. Mechanotransduction or cell signaling using mechanical forces is well known to be related to cell proliferation and growth (*10–14*), and is clinically applied in distraction osteogenesis for inducing bone growth (*15*), tissue expanders for producing skin grafts (*16*) and in wound healing (*17*). When healthy tissue of the desired type is present in the body, mechanically-induced growth can avoid many of the challenges of traditional tissue engineering, e.g., cell death prior to vascularization of the scaffold, immunogenic response to synthetic scaffolds, and mismatch between desired and actual tissue properties (*18–20*).

The lengthening of tubular organs, such as the esophagus, intestines and vasculature, is well suited to mechanically stimulated growth (*21–23*); though, the multifunctional nature of these organs, e.g., providing peristalsis and nutrient absorption, complicates the process in comparison to bone or skin. In addition, the approach in which growth-inducing forces are applied should not compromise current organ functionality by occluding flow (*22*) and, furthermore, should be minimally disabling to the patient, e.g., not require medically-induced sedation and paralysis as employed during treatments of esophageal atresia (*21*).

We report a robotic implant for tubular organ lengthening that addresses these challenges. It enables both automatic and operator-controlled mechanical force modulation based on sensor measurements of tissue displacement and force. The system serves as both a research tool for studying tissue-scale mechano-stimulation and as a precursor to a clinical device. We demonstrate the potential of robotically-induced tissue growth through in vivo porcine esophageal lengthening experiments during which the animals were awake, able to eat and move normally.

Results

We designed the robotic implant, first conceptualized in (*24*), to attach to the exterior of either disconnected or connected tubular organ segments (Fig. 1A,B) by two attachment rings. The implant body is positioned adjacent to the organ and is sized to avoid damage to surrounding tissue. It is covered in a smooth biocompatible waterproof skin that completely seals the interior motor, sensors and electronics from bodily fluids and enables gas sterilization (Fig. 1C,D). Traction is generated by translation of the lower attachment ring, which can move freely along the implant body due to the folds in the skin.

The open-ring geometry of the attachment rings (Fig. 1E) maintains the diameter of the lengthened organ while enabling attachment to both disconnected (Fig. 1A, esophageal atresia) and connected (Fig. 1B, bowel and vasculature) organ segments. Since the rings and implant are exterior to the organ, they do not occlude internal flow. The rings attach to the implant by sliding connectors allowing them to be first sutured to the organ without the implant obstructing the surgical field (Fig. 1F). To avoid the potential of creating a leak if a suture was to tear out of the tissue, the sutures are placed so that they do not penetrate the organ lumen.

The implant was designed such that the only forces it generates are equal, opposite and collinear forces applied to the tubular organ (Fig. 1A,B). This strategy decouples traction forces from the

patient's physiological movement to avoid the risks and lifestyle impairment associated with some current techniques. For example, in the clinical treatment of long-gap esophageal atresia, forces applied to the esophageal segments are generated via passive reaction forces on the patient's back (Fig. 1G) (*21*). Patients are maintained in a state of sedation and paralysis in the ICU for the duration of traction (1-4 weeks) so that the sutures do not tear out of the esophagus due to musculoskeletal motion.

The implant body contains a motor that controls the position of the lower ring, as well as sensors that measure the distance between the rings and the force on the lower ring (Fig. 1D). The implant's microcontroller, communication chip, and battery power supply are located in a wearable control unit outside the host, which is connected by cable to the implant body (Figs. 2A,4D). The microcontroller was programmed to provide a variety of functionality. For the studies reported here, a basic control mode was used in which the force applied by the rings or the distance between them could be commanded wirelessly from a laptop computer that is also used for data logging and visualization (Fig. 2A). This mode was used for two reasons. First, we wanted to mimic the daily fixed displacements of clinical practice. Second, for reasons of animal safety in testing a new device, we wanted to be present to ensure the animal was not undergoing distress when traction was adjusted. More complex robotic control is also possible, such as removing the applied force when the implant detects that the animal is feeding.

We experimentally verified the capability of the robotic implant to induce tubular tissue growth on healthy connected esophagus in swine. This approach combines the more stringent implant size requirement of esophageal lengthening (Fig. 1A) with evaluation of the organ's transport ability during traction as is necessary during bowel lengthening (Fig. 1B). Two groups of animals were used: a surgical group (n=5) that received the implant, and a naïve group (n=3) that did not. In the surgical group, the rings were sutured to the esophagus at an initial separation distance of 20.2 +/- 0.8mm. To track esophageal lengthening outside the traction zone, e.g., due to animal growth, control segments were marked 20mm proximal and 20mm distal to the attachment rings using pairs of X-ray-visible surgical clips. Each pair of clips marked a ~20mm segment. In this way, each animal acted as its own control so that tissue changes due to the presence of the implant could be distinguished from changes due to applied force.

Traction was started two days after implantation (Day 2) and ring separation distance was increased by an average of 2.5mm each day (Fig. 2B) through Day 9 (n=2) or Day 10 (n=3). Following a rapid increase in ring separation distance, the measured force was observed to increase equally rapidly and then decrease following an approximately exponential decay over the subsequent 24-hour period (Fig. 2B). The daily ring displacement, however, ensured that the force and strain on the loaded segment did not reach zero owing to the lengthening that occurs over the subsequent 24-hour period. Note that the force spikes in Fig. 2B occurring at 7:30AM and 4PM correspond to meal times when the pig was eating.

The animals did not display any signs of discomfort due to adjustment and fluoroscopic examination indicated normal flow through the stretched region (Fig. 2C, Movie S1). Furthermore, all animals expressed normal appetite, consumed the provided amount of food (based on animal weight and age) and passed stool. Despite having undergone a major surgery, all animals gained weight (weight gain of 2.2 +/- 1.3 kg).

The implant-reported distance between the rings was in agreement with the distance as derived from X-ray and fluoroscopic images taken to assess the adjustments on Days 0 and 4, and on the final day (Day 10 or 11) (Fig. 2D).

On the final day, to measure total elongation in vivo, we iteratively adjusted the ring separation distance to remove the residual force and strain and then recorded the corresponding ring distance. The distances before and after removal of residual strain are shown in Fig. 2D. The zero-strain length increased by 77 +/- 13% (mean ± standard deviation), over the 8-9 days of force application. These measurements, which were in agreement with physical measurements taken at necropsy (Fig. 2E), demonstrated a statistically significant increase with respect to the clip-marked esophageal sections above and below the implant, which increased in length by 10 +/- 12%.

In congruity with clinical practice, a fibrous capsule (Fig. 4E) formed around the silastic sheet (Fig. 4C) enveloping the implant and esophagus. The capsule was found to be easily removable from both the implant and the esophagus.

While esophageal lengthening is performed clinically, there is controversy as to whether the esophageal segments are growing or simply stretching (*25*). To investigate this, we first studied the geometry of the lengthened samples. The excised esophagi were cut longitudinally and unrolled showing a healthy appearance of the mucosa (Fig. 2E). The tissue width (esophagus circumference) measured 8.2 +/- 1.4mm between the rings and 8.9 ± 1.5mm and 8.7 ± 2.1mm in the proximal and distal control segments, respectively, indicating that the tissue is uniform along the entire length and elongation has preserved lumen diameter within a fraction of a millimeter.

The cross section of the esophagus is comprised of five tissue layers (Fig. 3A): the muscularis externa, submucosa, muscularis mucosa, lamina propria and epithelium (*26*). The muscularis externa is the thickest layer and is comprised of a mixture of skeletal and smooth muscle cells arranged in longitudinal and circular sublayers. The structure of this layer facilitates investigation into whether lengthening is due to growing or stretching, as described below.

To measure how the thickness of this layer may have changed, we studied tissue samples stained with Masson's trichrome. Statistical analysis shows that the thickness of the lengthened muscular layer was preserved with respect to the adjacent control segments and also with respect to tissue taken from the naïve group (Figure 5A).

Since both the circumference and thickness of the muscularis externa are maintained during lengthening, its volume has increased. Further testing was performed to understand if this volume increase was due to cellular hypertrophy, proliferation, the generation of fibrosis or a combination of these effects.

To explore if lengthening could be attributed to muscle cell hypertrophy, we compared skeletal muscle fiber cross section in both circular and longitudinal muscle layers of the muscularis externa (Fig. 3B). We found no statistically significant difference in fiber cross section between the lengthened tissue and tissue collected from the set of naïve swine indicating that lengthening is not due to muscle hypertrophy (Fig 5B).

We also used DAPI immunofluorescent staining to compare the nuclear density of the muscularis externa in the surgical group with naïve swine tissue (Fig. 3C) and found no statistically significant difference (Fig. 5C). The observed trend of increasing nuclear density from proximal to distal segments can be explained as follows. The muscular layers in the esophagus are a mixture of skeletal and smooth muscle cells. The ratio of skeletal to smooth cells varies along its length with a larger proportion of skeletal muscle cells in the proximal region and a smaller proportion in the distal region. Smooth muscle has a larger number of nuclei than skeletal muscle and so the observed variation in nuclear density is to be expected.

We also quantified the nuclear density of the inner epithelial layer, which does not vary in composition along the esophageal length. No statistical difference in nuclear density was found between the three regions of the surgical and naïve groups (Fig. 5D).

As a definitive demonstration of cellular proliferation, we compared nuclear proliferation in the muscle cells of the muscularis externa using a Ki67 and Desmin staining protocol. We observed a statistically significant increase in proliferation of muscle cells in the lengthened tissue compared to tissue from the naïve group (Fig. 5E).

All of these results indicate that tissue growth has occurred. To quantify in the muscle layers what fraction of lengthening is due to muscle cell proliferation and what fraction is due to fibrosis, Masson's trichrome staining was used to quantify the relative fraction of muscle and collagen measured by area (Fig. 3D). In the naïve animal tissue, the muscle / collagen ratio was 93% / 7%. In the lengthened segments, the muscle / collagen ratio was 80% / 20% (Fig. 5F). As detailed in Materials and Methods, since the collagen is interspersed between groups of muscle cells, these ratios can be used to divide the average lengthening of 77% into components due to muscle cell proliferation (49%) and collagen proliferation (28%). Put another way, 63% of lengthening is due to muscle cell proliferation and 37% is due to collagen formation (compared to 93% / 7% if the original ratio of muscle / collagen had been maintained).

Discussion

These are the first results to demonstrate in a large animal model that esophageal traction-induced lengthening is not due to stretching (change in cross section dimensions or cellular hypertrophy), but rather a combination of cellular proliferation and fibrosis.

Our robotic implant establishes that lengthening of tubular organs can be achieved in a precisely controlled manner that maintains organ geometry, preserves organ functionality, and eliminates the need for patient immobilization during growth. Furthermore, by exploiting tissue-level mechano-stimulation, the standard challenges of tissue engineering are avoided.

Robotic implants offer substantial benefits compared to the static approaches currently applied to esophageal, bone and skin growth. This includes the capability to apply dynamic time-varying strains based on the physiological processes of the tissue. In clinical practice, strain adjustments for esophageal, bone and tissue expansion are performed in discrete steps on a daily or weekly basis. Such clinical regimens, as reproduced in the experiments reported here, do induce organ growth, but can also alter tissue properties, e.g., produce fibrosis. It is well known, however, that tissue responds not only to static strains, but also to dynamic loading. Examples from tissue engineering include skeletal muscle (*27*), smooth muscle (*28*), cartilage (*29*) and arteries (*30*). Furthermore, periodic relaxation of traction may enhance tissue perfusion. And while mechanotransduction has been studied on the cellular level (*10,11*), little is known at the organ level about the mechanisms governing mechano-stimulated organ growth. Robotics provides the capability to study these mechanisms and to apply what is learned clinically in order to optimize organ morphology, function and growth rate.

Robotics also provides the ability to respond autonomously to changes in the biological system. A simple example is adapting the adjustment of strain to accommodate actual growth during the lengthening process. Some existing methods adjust tissue loading by the same amount every day – resulting in a daily decrease in applied strain as the tissue lengthens. In other cases, e.g., skin expansion, the amount of adjustment is based on palpation to assess tissue tightness and perfusion. A force- or pressure-sensing robotic device can be programmed to consistently provide the desired level of strain by regularly recalibrating itself to account for actual growth.

More complex interaction with the biological host is also possible, such as removing the applied strain when the implant senses specific physiological activity. For example, in our porcine experiments, it was possible to detect when the animal was eating based on force spikes (Fig. 2B). While our monitoring of the animals indicated that the applied strain did not cause them discomfort while swallowing, the robotic implant could have removed the applied force until it sensed that the animal had finished eating. Similarly, in bowel lengthening, a robotic implant could be programmed to detect peristalsis and relax for a period of time to facilitate passage of food.

While robotics can significantly enhance mechano-stimulated organ growth, there are potential limitations to what it can achieve. For example, long-gap esophageal atresia, as a congenital condition, is treated when patients are children and growing. While bone lengthening and skin expansion are performed successfully in adults, it is unknown whether the mechanisms that induce lengthening in the pediatric esophagus are still active in adults. Furthermore, the nerves controlling esophageal contraction run along its length. In cases of esophageal atresia, the nerves are interrupted and do not fully regenerate after anastomosis. Despite impaired peristalsis, however, the repaired esophagus, aided by gravity in humans, successfully performs its main function as a conduit to the stomach. In our swine studies, the continued effectiveness of the esophagus was demonstrated by normal function of the alimentary canal and by animal weight gain. Even if esophageal motility were to have some impairment from growth induction, the ability to achieve an intact esophageal conduit would remain preferable to surgical alternatives such as esophageal replacement where normal esophageal motility would clearly not be expected.

Beyond their use for organ growth, robotic implants represent a new direction in medical robotics. These bionic systems can assist in performing normal body functions either temporarily, until the body repairs itself, or permanently. The ongoing miniaturization of sensors (*31*) and actuators (*32*) together with the continuing development of techniques for wireless communication, power transfer (*33*, *34*) and energy scavenging (*35*) may lead to devices surpassing even those proposed in science fiction.

Materials and Methods

Robot Design

The structural components of the robot are fabricated from stiff waterproof polymers (Fig. 1D). These consist of the rack (machined delrin, reinforced with a 1/16” diameter stainless steel rod) and two end caps molded from urethane resin (Smooth-Cast ONYX Slow, Reynolds Advanced Materials). Three additional stainless steel rods (1/16” diameter) attached to the two caps act as an endoskeleton to stiffen the frame and also to prevent surrounding tissue from herniating into the mechanism.

The robotic mechanism is comprised of a machined aluminium carriage that slides along the rack under the control of a motor-driven (298:1 gear box, 40 oz-in torque, Pololu Corp.) worm gear (A1C55-N24, SDP/SI). The worm gear is nonbackdriveable, meaning that when the motor is turned off, the position of the carriage does not change. A potentiometer (652-3266W-1-103LF, Bourns Inc.) rotating with the worm gear, measures displacement of the carriage along the rack, and is fixed to a steel frame (polished gray steel, Shapeways) that attaches to the carriage. The lower ring is attached to the carriage by a hinge joint that transmits the tensile force applied by the tissue on the ring to a force sensor (FSS Low Profile Force Sensors, FSS1500NST, Honeywell Inc.) mounted on the carriage.

The tubular organ is attached to the implant by two rings (Fig. 1C-F). Six sutures spaced equally about the circumference are used to attach each ring to the esophagus. The design is intended to provide uniform distribution of traction forces around the organ's circumference to support tubular growth and to minimize the chance of the sutures tearing out of the tissue. The rings are fabricated from welded 1/16" diameter stainless steel rod stock. The open ring design enables attachment to connected organs and adjustment of ring diameter (Fig. 1E). Grooves on the outer surface of the ring prevent suture from sliding along or off the ring. To enable the rings to be first sutured to the organ and then attached to the implant, each ring includes a U-shaped connector. This connector slides onto a mating T-shaped stainless steel connector located on the outside of implant's encapsulation (Fig. 1E,F).

Robot Encapsulation

The robot mechanism and electronics are completely sealed inside a biocompatible medical-grade encapsulation that permits sterilization using ethylene oxide. The main encapsulation component is a 0.070" thick cylindrical silastic skin (PR72034-007R, Bentec Medical) that is reinforced with an embedded polyester mesh. Rather than being stretched taut between the end caps, excess material is used to create folds on each side of the moving attachment ring (Fig.1C). This allows the ring to translate along the implant body without stretching the silastic skin – which would interfere with ring force measurement and also increase required motor torque. Molded silastic caps (MDX4-4210, Dow Corning Corp.) seal each end of the cylindrical skin. Electrical conductors are encased in a 20Fr silastic tube (GS75160-20, Bentec Medical) integrated with the bottom cap and attached to Ethernet connectors. The I-shaped connectors for the tissue attachment rings are clamped to the underlying mechanism by screws that pass through the encapsulation. These attachments as well as all joints of the encapsulation were sealed using a medical-grade silicone adhesive (Type A, Dow Corning Corp.). The weight of the encapsulated implant is 99.4g and the rings weigh 3.5g.

Control and Communication

The implant is connected by cable to a wearable control unit located outside the body that integrates all circuitry related to control, sensing and communication with a battery power supply (Figs. 2A,4D). The main electronic components are a microcontroller (Baby Orangutan B-328, Pololu Corp.), a differential amplifier (MCP6001, Microchip Technology, Inc) for the force sensor, a voltage regulator, and a Bluetooth transmitter module (Blue Smirf Silver, Sparkfun Electronics). The power supply consisted of four 9V batteries connected in parallel. A low-level controller, programmed in C++, uses Proportional Integral Derivative (PID) control to position the moving attachment ring to achieve control commands consisting of either a desired ring-to-ring spacing or desired ring force. Control commands are received via Bluetooth from a laptop computer. These commands can be entered individually or can be preprogrammed to produce a desired waveform, e.g., adjustment once per day or every few minutes. Sensor data is streamed to the laptop by Bluetooth at a sampling frequency of 6.6Hz. A graphical user interface on the laptop allows real time data plotting, control command entry, controller gain adjustment and emergency stopping of the motor.

Animal Groups

Two animal groups were used in these experiments. Both groups were comprised of young Yorkshire female pigs of approximately the same weight (43.5 +/- 3.7 kg, mean mass ± one standard deviation) and age (14.4 +/- 1.0 weeks). The *surgical* group (n=5) underwent esophageal lengthening as described below. Within this group, 3 animals underwent 9 days of lengthening and

2 animals underwent 8 days of lengthening. The difference in duration was due solely to procedure scheduling constraints. The *naïve* control group (n=3) underwent no surgical procedure. For both groups, tissue samples were collected immediately following animal sacrifice.

Surgical Procedure and Animal Care

The surgical procedure is inspired by the Foker technique for the clinical treatment of long-gap esophageal atresia (Fig. 1G) (*21*). In this technique, suture loops are attached to the ends of the esophagus and passed through intercostal spaces to be tied off against force-distributing buttons positioned on the baby's back. Suture force is manually increased each day by inserting short lengths of millimeter-diameter tubing between the suture loops and buttons. During the 1-4 weeks of traction, patients are maintained in a state of sedation and paralysis in the Intensive Care Unit (ICU) so that the sutures do not tear out of the esophagus due to musculoskeletal motion.

Animal care followed procedures prescribed by the Institutional Animal Care and Use Committee. After induction of anesthesia, the animal was intubated and placed on ventilation. A right thoracotomy was performed at the 7th intercostal space and the esophagus was dissected from the surrounding adventitia. A tunnel was created at the 9th intercostal space and the implant cable was passed through it and connected to the control box. Keeping the implant body within the sterile field, but outside the surgical cavity, the two attachment rings were sutured to the esophagus at a nominal separation distance of 20mm (Fig. 4A). Additionally, two pairs of titanium clips (LIGACLIP® Extra Ligating Clips, LT300, Ethicon LLC.) were placed 20mm proximal and distal to the rings. The clips in each pair were placed 20mm apart to provide the means to track lengthening of the esophagus outside the traction region. These segments are referred to as the *proximal control segment* and the *distal control segment*.

Subsequently, the robot was placed in the right thorax and attached to the rings (Fig. 4A). To prevent adhesions of the esophagus to surrounding tissue as well as to protect the lungs, a silastic sheet (PR72034-007R, Bentec Medical) was wrapped around the dissected esophagus and implant (Fig. 4B). The sheet was sutured to itself forming a cylinder and also sutured to the esophagus to prevent it from sliding along the organ (Fig. 4C). The right thorax was closed in three layers. Two chest tubes were used to remove air from the pleural cavity.

Patency of the esophagus and operability of the implant were assessed immediately after surgery using X-ray or fluoroscopy. The pig was then dressed in a vest (SAI Infusion Technologies) containing a zippered pocket on its back into which the control unit and batteries were placed. The animal was then weaned from anesthesia. During the subsequent days of the experiment, the animals were fed three times per day with a slurry diet consisting of milled grains, water and juices. They also received Omeprazole (to limit stomach acid), Cephalexin (antibiotic) and Fentanyl (pain reliever). The batteries were changed once per day. The animals gained 2.2 +/- 1.3 kg in weight between surgery and sacrifice. In addition to immediately after surgery, imaging was also performed on day 4 and on the final day (10 or 11).

Daily Implant Adjustment

After allowing the animals to recover for one full day, traction was initiated on the morning of Day 2. During this first traction adjustment, the rings were advanced sufficiently to apply a force of ~2N to the segment between the rings. This corresponded to an average displacement of 7.2 ± 2.4mm. Subsequent adjustments were performed each morning at approximately the same time (9:00 am) with the distance between the rings increased by an average of 2.5mm per day (Figs. 2B,2D).

Segment Length Measurement

The implant provided continuous length measurement of the segment undergoing traction. X-ray and fluoroscopic images taken on Days 0, 4 and the final day (Day 10 or11) were used to measure the length of the proximal and distal control segments. Prior to sacrifice, the implant was adjusted in an iterative fashion to remove the traction force from the lengthened segment. This was performed over a 10-15 minute period to allow for tissue relaxation. The ring distance corresponding to zero force was taken as the final segment length. These measurements were in good agreement with manual measurements of the excised tissue. The lengths of the control segments and stretched segment are plotted in Fig. 2D. The data for the proximal control segment in one animal was discarded since the measurement indicated that at least one of the clips had become detached from the esophagus.

Physical Measurement of Lumen Diameter

To measure the lumen diameter, the wall of the excised esophagus was cut longitudinally and unrolled to a rectangular shape (Fig. 2E). Width measurements of the esophagus in this configuration represent the circumference of the lumen.

An image was taken of each esophagus with a ruler next to it. Using ImageJ (National Institutes of Health), 20 width measurements were made for each of the three segments of interest (proximal control, lengthened and distal control) in the surgical group. Sixty measurements of width were taken for each esophagus in the naïve group. Average lumen circumferences were computed from these data sets.

Histology

Esophageal tissue samples were collected from each animal in the surgical and naïve groups. Both longitudinal and transverse samples were prepared by fixing in 10% neutral-buffered formalin and then embedded in paraffin. Sections were cut and stained with Masson's trichrome using routine histological protocols. DAPI fluorescent staining was used for characterizing nuclear density. To quantify muscle cell proliferation, a double stain protocol was developed for porcine esophagus using anti-desmin protein antibody (D8281, Sigma-Aldrich; 1:4000 dilution) and the Ki-67 antibody (VP-RM04, Vector Labs; 1:250 dilution). Sequential double staining was performed on the Leica Bond III staining platform. Antigen retrieval was performed using Bond Epitope Retrieval 1 for 30 minutes. Ki-67 was detected and developed using Bond Polymer Refine Detection Kit, and Desmin was detected and developed using Bond Polymer Refine Red Detection Kit.

Specimens were visualized using a microscope (BX53, Olympus America Inc.) and image acquisition was carried out using AxioVision Microscopy Software (v. 4.8.2, Carl Zeiss Microscopy) and ImageScope (v. 12.3.0.5056, Leica Biosystems GmbH).

Thickness of the Muscularis Externa

To measure layer thickness, longitudinally-cut Masson's trichrome stained samples were used. Three images at 5X magnification, evenly spaced along the length of the tissue, were taken. The filenames were blinded using an MD5 hash before being measured. Twenty evenly spaced measurements were taken using ImageJ in each of the 3 images resulting in 60 measurements per slide for each layer. These measurements were then averaged. A t-test was used to compare surgical and naïve control groups. The results are presented in Fig. 5A.

Muscle Fiber Diameter

To investigate cell hypertrophy, a study of skeletal muscle fiber cross sectional diameter was performed. Skeletal muscle fibers are clearly visible on Desmin stained slides and are arranged in both longitudinal and circular layers in the muscularis externa. Fiber diameters were compared since they are less sensitive to sample cutting angle than fiber length. Four longitudinally cut tissue samples were used for the circular muscle layer and 4 circumferentially-cut tissue samples were used to measure the longitudinal muscle layer. Using ImageJ, the two maximally distant points of each fiber cross section were selected manually and the software computed the distance between them (Fig. 3B). An average of 120 muscle cell diameters were counted per pig (min 75, max 175). The averages are shown in Fig. 5B. A t-test was used to compare surgical and naïve control groups. There was no significant difference in skeletal fiber diameter for either the circular muscle layer or the longitudinal muscle layer.

Nuclear Density

Longitudinally-cut tissue samples stained with DAPI immunofluorescent stain were used to quantify nuclear density. Up to twelve 10X magnification images were used when possible depending on the amount of available tissue. If the full area of the layer was covered in less than twelve fields of view, then only as many images were required to cover the entire area of the layer were used. The minimum number of fields used in any one animal was six, and the minimum number of nuclei counted was 1484.

A morphological algorithm was written in Python and openCV to count the number of nuclei in each image. Nuclei had a variety of shapes and sizes, and some nuclei appeared in clusters of 20 or more. The algorithm was designed to compensate for these challenges. First, all DAPI positive contours in the image were identified. Contours were then sorted to eliminate those falling outside minimum and maximum size constraints (based on manual identification of the largest and smallest nuclei in the full data set). The mean nucleus size and standard deviation were then computed from the reduced contour list. All contours were then divided into one of two categories: (1) Single nucleus if the area of the contour is less than the median or larger than the median but higher than 84% circularity, (2) Multi-nucleus cluster if area is larger than median area, smaller than median area plus 2 standard deviations and low circularity, or if area is larger than median area plus 2 standard deviations. The number of nuclei in a multi-nucleus cluster was estimated according to the following equation: $\#\,nuclei = round(\frac{Cluster\ Area}{Mean\ Nucleus\ Area})$. This algorithm gave good agreement with manual counting on sample images.

The nuclear density of both the lengthened and naïve samples was observed to increase along the length of the esophagus. This corresponds to the increasing ratio of smooth to skeletal muscle cells along the length of the esophagus. Smooth muscle cell clusters have a much higher nuclear density than skeletal muscle cells leading to higher densities at distal locations. Based on a t-test, comparisons of the densities of the lengthened and naïve tissue segments in each of the three sections show that they are not statistically different.

Nuclear Proliferation at Time of Sacrifice

To provide a direct measurement of cell proliferation at the time of sacrifice, we used a dual Ki67 and Desmin staining protocol to both detect proliferating nuclei and to be able to associate nuclei with muscle cells. We computed the percentage of Ki67-marked muscle-cell nuclei in the muscularis externa in the surgical and naïve groups.

Longitudinal tissue samples were used to quantify nuclear proliferation. Eight images at 32X magnification were used. Total nuclei were counted from the digital photographs of these fields.

The names of the files were blinded before counting. Ki67-marked nuclei were counted blind through the eyepiece of the microscope, as a high fidelity of color was required to distinguish proliferating cells from nonproliferating cells. The percentage of proliferating muscle nuclei was shown to be larger in the surgical group compared to the naïve group (Fig. 5E) as computed with the Mann-Whitney U-test.

Percentage of Lengthening Due to Muscle versus Collagen (Fibrosis)

The muscularis externa is composed of groups of smooth and skeletal muscle cells interconnected by collagen, as seen in Fig. 3D. Given this structure, tissue along the direction of lengthening is comprised partially of muscle and partly of collagen. To compute how much of the lengthening was due to muscle cell proliferation and how much was due to collagen proliferation, we considered lines parallel to the direction of elongation and measured the ratio of the lengths of the cell types intersecting these lines. Computing the average ratio over all possible lines in a tissue region is equivalent to computing the ratio of cell-type areas in that region.

We used longitudinal Masson's Trichrome-stained tissue samples from the lengthened segments in the surgical group and from the naïve group. Eight, 10X magnification images of the muscularis externa were obtained if sufficient tissue was available on a slide. If the full area of the layer was covered in less than eight fields of view, then only as many images as were required to cover the entire area of the layer were used (minimum fields used was 3).

For each animal, a set of three color thresholds in the HSV color space were chosen. Red represented muscle, blue represented collagen and white represented a void of tissue in the image. Once the thresholds were set, an algorithm written in Python and OpenCV was used to threshold each image into three parts, removed the tissue voids, and tallied the area of each tissue type.

Using this method, the muscle / collagen ratio of naïve tissue was found to be 93% / 7%. In lengthened tissue, the muscle / collagen ratio was 80% / 20% (Fig. 5F). Since the ratio changed, we need to solve a set of linear equations to determine the fraction of lengthening due to muscle cell proliferation versus the fraction due to collagen proliferation. Defining the following variables,

L^i = total initial tissue segment length

δ = increase in tissue segment length

$l_m^i = 0.93\,L^i$ = initial length comprised of muscle cells (measured in naïve tissue)

$l_c^i = 0.07L^i$ = initial length comprised of collagen (measured in naïve tissue)

$l_m^f = 0.8\left(L^i + \delta\right)$ = final length comprised of muscle cells

$l_c^f = 0.2\left(L^i + \delta\right)$ = final length comprised of collagen

we can solve for the lengthening due to muscle and collagen proliferation using the following equations:

$$\frac{\left(l_m^f - l_m^i\right)}{L^i} = \frac{\left(0.8\left(L^i + \delta\right) - 0.93L^i\right)}{L^i} = 0.8(0.77) - 0.13 = 0.49$$

$$\frac{\left(l_c^f - l_c^i\right)}{L^i} = \frac{\left(0.2\left(L^i + \delta\right) - 0.07L^i\right)}{L^i} = 0.2(0.77) + 0.13 = 0.28$$

These numbers indicate the segment lengthening due to muscle proliferation alone (49%) and collagen proliferation alone (28%) with their sum yielding the total observed lengthening of 77%. We can also express these numbers as fractions of the total 77% lengthening,

$$\frac{\left(\frac{\left(l_m^f - l_m^i\right)}{L^i}\right)}{\left(\frac{\delta}{L^i}\right)} = \frac{0.49}{0.77} = 0.63$$

$$\frac{\left(\frac{\left(l_c^f - l_c^i\right)}{L^i}\right)}{\left(\frac{\delta}{L^i}\right)} = \frac{0.28}{0.77} = 0.37$$

These numbers indicate that 63% of lengthening was due to muscle cell proliferation and 37% was due to collagen proliferation.

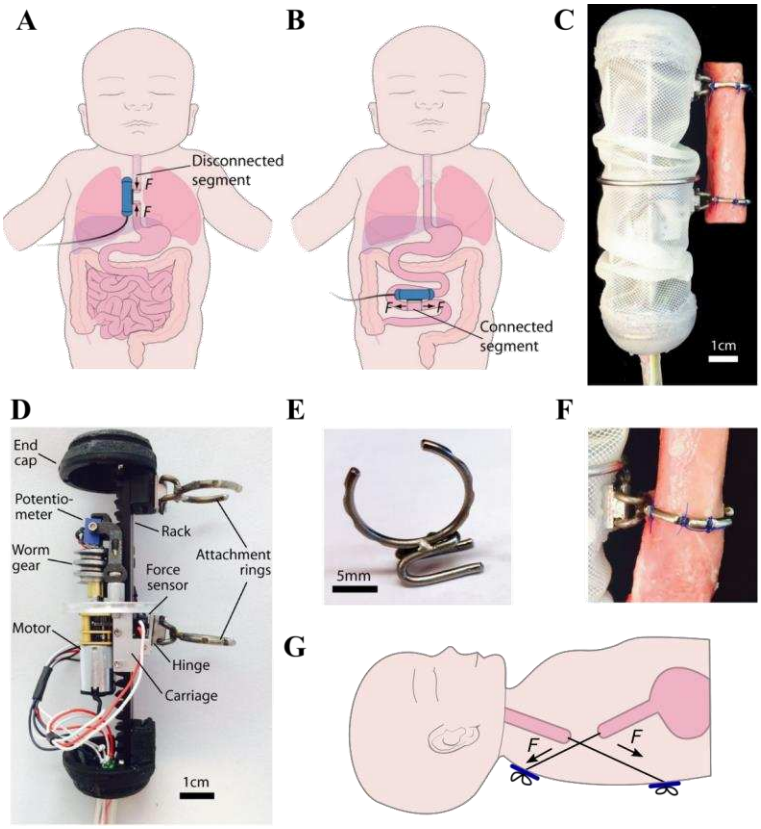

Fig1. Robotic implant for tubular tissue growth. (**A**) Long-gap esophageal atresia – Implant applies forces, *F*, to disconnected esophageal segments. After inducing sufficient growth, the segments are surgically connected to form a complete esophagus. (**B**) Short bowel syndrome – Implant applies forces, *F*, to connected segment of bowel. By inducing sufficient lengthening to support the absorption of necessary calories and fluids, a dependence on intravenous feeding can be eliminated. (**C**) Robot is covered by biocompatible waterproof skin and is attached to tubular organ by two rings (esophageal segment shown). Upper ring is fixed to robot body while lower ring translates along body. (**D**) Robot with skin removed to show motor drive system and sensors. Rotation of worm gear causes lower ring to translate along body. (**E**) Rings detach from robot body to facilitate attachment to tubular organ. (**F**) Tissue is attached to the ring using sutures. (**G**) Foker technique for treating long-gap esophageal atresia (*21*) – Sutures externalized on the patient's back are used to apply forces, *F*, to esophageal segments.

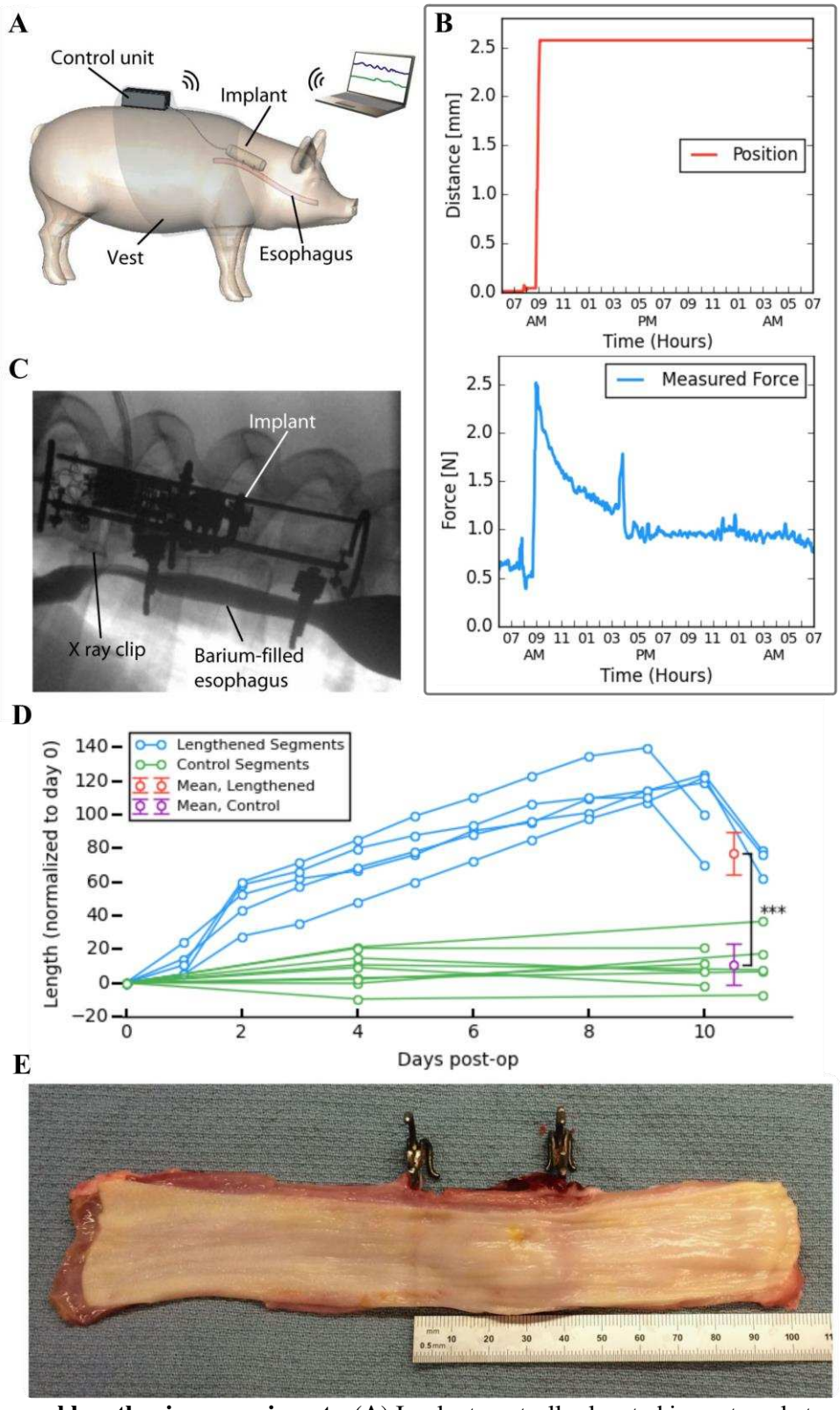

Fig 2. Esophageal lengthening experiments. (**A**) Implant controller located in vest pocket communicates wirelessly with laptop computer. (**B**) Force and position data recorded over a 24-hour period. (**C**) Fluoroscopic image showing flow of contrast agent through esophagus during traction. (**D**) Esophageal segment length versus time. Surgery occurs on Day 0. Segment length corresponds to distance between

implant attachment rings for lengthened segment (blue) and distance between clips for control segments (green). Average values at midpoint fluoroscopy and sacrifice are given (in red and purple, respectively). Two animals were survived to Day 10 and three were survived to Day 11. *** p<0.0001. (**E**) Resected esophagus cut along its length and unrolled along its circumference to show epithelium. Rings are placed adjacent to attachment locations for reference. Note normal appearance of tissue and uniform diameter of lengthened section.

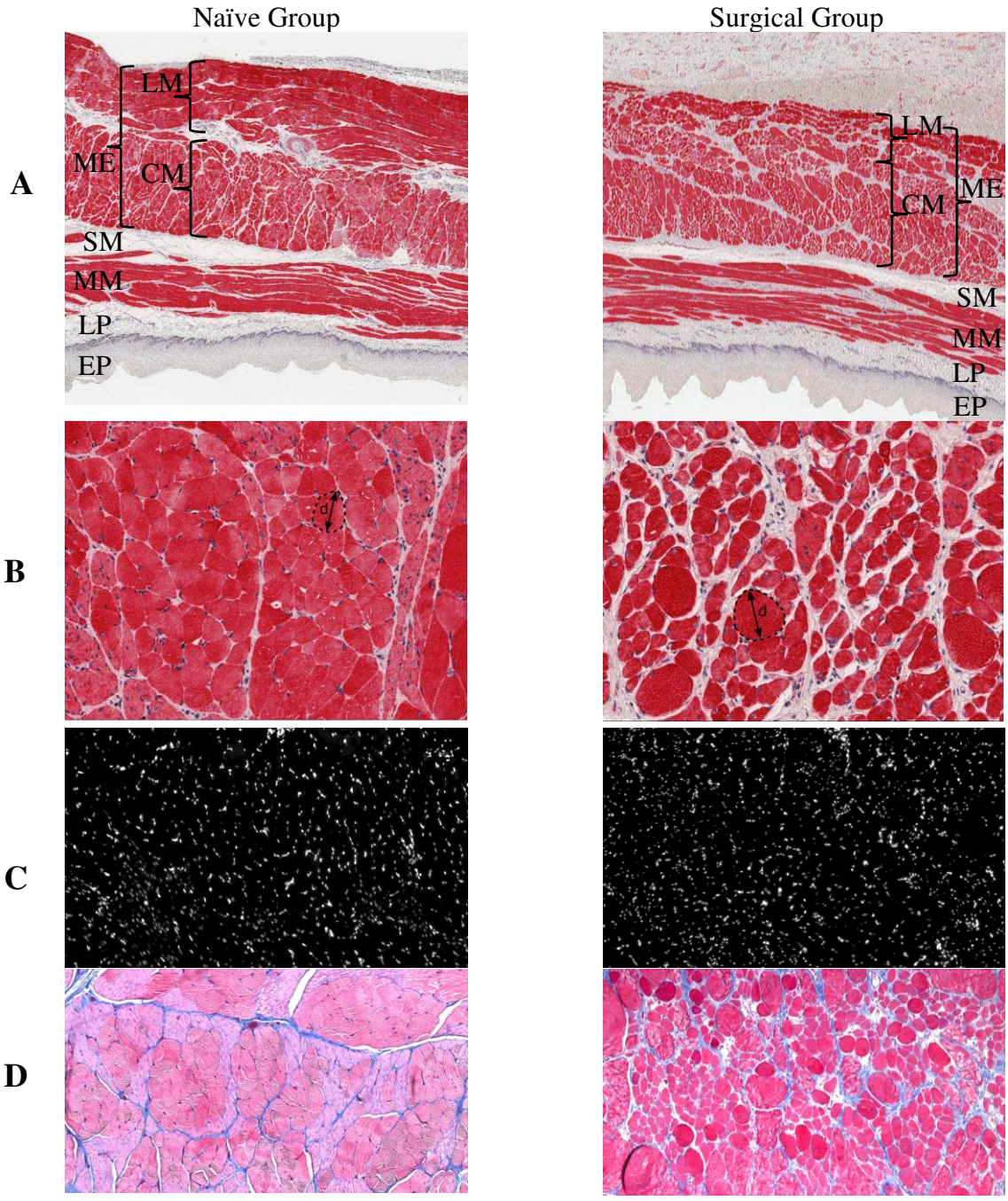

Fig 3. Esophageal tissue histology. (**A**) Longitudinal sections of Desmin stained tissue (1X magnification) showing tissue layers: Muscularis Externa (ME), comprised of Longitudinal Muscle (LM) and Circular Muscle (CM); Submucosa (SM); Muscularis Mucosa (MM); Lamina Propria (LP); and

Epithelium (EP). (**B**) Longitudinal sections of Desmin stained tissue (20X magnification) illustrating diameter measurement of skeletal muscle fiber cross sections. (**C**) Longitudinal sections of DAPI stained tissue (10X magnification) used to assess nuclear density. (**D**) Longitudinal sections of Masson's trichrome stained tissue (20X magnification) for measuring relative fractions of muscle (pink) and collagen (blue).

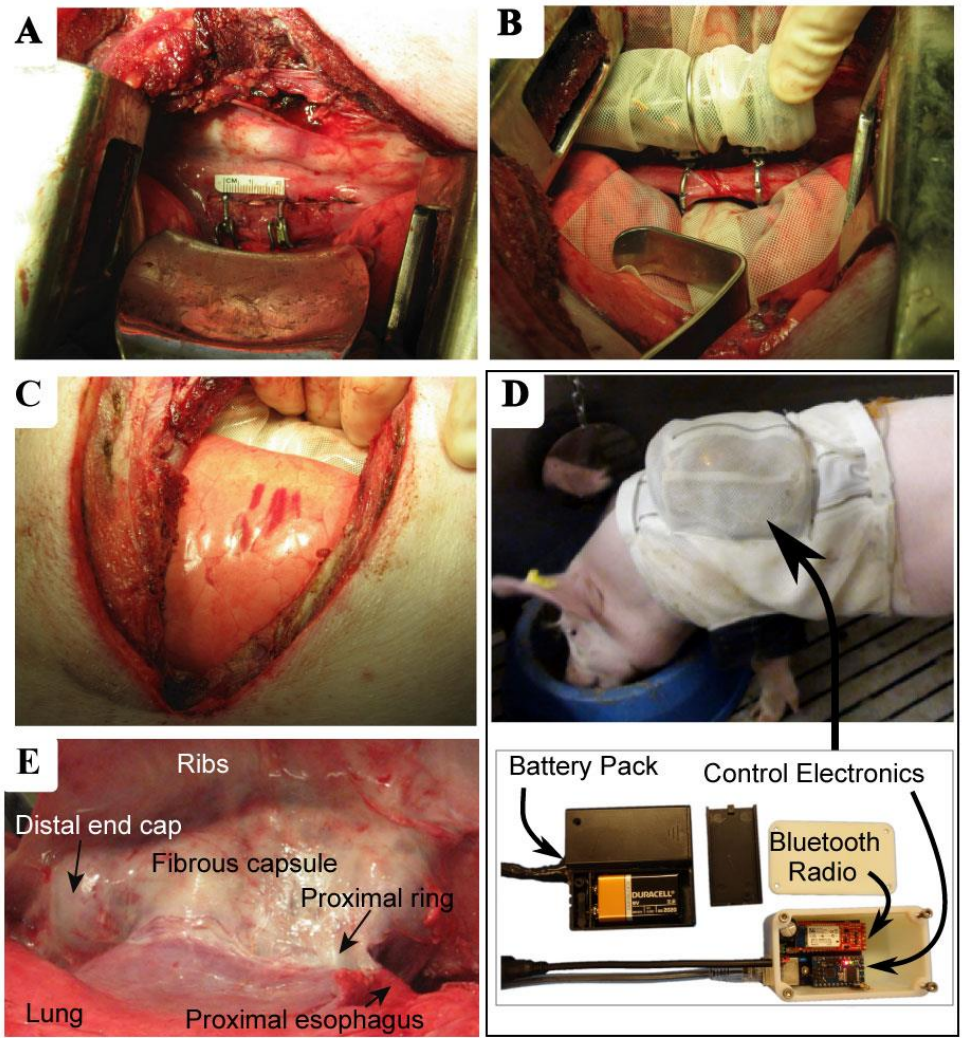

Fig. 4. Implant surgery. (**A**) Suturing of rings to esophagus. (**B**) Silicone sheet is inserted behind esophagus and implant is connected to attachment rings. (**C**) Implant and esophagus, wrapped in silicone sheet, positioned between the rib cage and right lung prior to surgical closure. (**D**) Control electronics are housed in a vest pocket. (E) Necropsy view of fibrotic capsule surrounding implant. Bulges due to proximal ring and distal end cap can be seen in capsule.

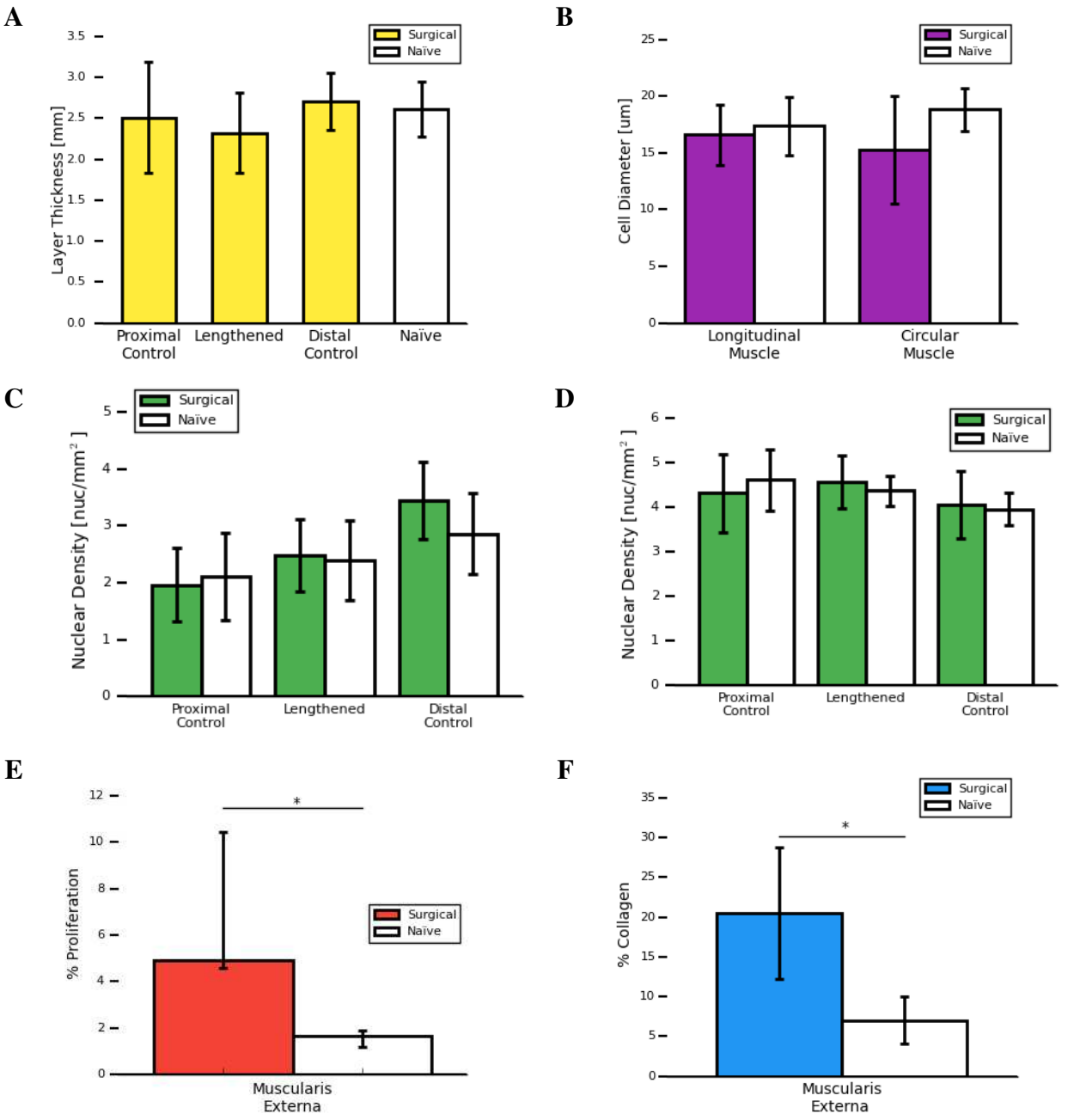

Fig. 5. Histology results comparing surgical and naïve groups. Asterisks indicate p-values less than 0.05 with specific values given in subcaptions. Error bars indicate one standard deviation unless otherwise noted. (**A**) Thickness of muscularis externa. (**B**) Skeletal muscle fiber diameter in longitudinal and circular layers of muscularis externa comparing lengthened surgical and naïve segments. (**C**) Nuclear density of muscularis externa. (**D**) Nuclear density in epithelium. (**E**) Median percentage proliferating muscle cells in muscularis externa of lengthened surgical segment versus naïve tissue. Error bars represent first and third quartiles (*p=0.025*). (**F**) Percentage of collagen in lengthened surgical segment versus naïve tissue. (*p=0.002*)

Movie 1

Fluoroscopic video shows in vivo adjustment of implant consisting of increase in segment length of 2mm. Barium is administered before and after adjustment to assess patency of the esophagus.

References and Notes:

1. N. P. Wiklund, Technology Insight: surgical robots—expensive toys or the future of urologic surgery? *Nat. Clin. Pr. Urol.* **1**, 97–102 (2004).
2. K. P. Sajadi, H. B. Goldman, Robotic pelvic organ prolapse surgery. *Nat. Rev. Urol.* **12**, 216–24 (2015).
3. G.B. Prang, M. J. Jannink, C. G. Groothuis-Oudshoorn, H. J. Hermens, M.J. IJzerman, Systematic review of the effect of robot-aided therapy on recovery of the hemiparetic arm after stroke. *J. Rehabil. Res. Dev.* **43,** 71 (2006).
4. C. L. Massie *et al.*, A clinically relevant method of analyzing continuous change in robotic upper extremity chronic stroke rehabilitation. *Neuorehabil. Neural Repair.* **30,** 703-712 (2016).
5. M. Goldfarb, B. E. Lawson, A. H. Shultz, Realizing the promise of robotic leg prostheses. *Sci. Transl. Med.* **5**, 210ps15 (2013).
6. L. Resnik, K. L. Shana, E. Klinger, The DEKA Arm: Its features, functionality, and evolution during the Veterans Affairs Study to optimize the DEKA Arm. *Prosthet. Orthot. Int.***38,** 492-504 (2014).
7. W. Cornwell, In pursuit of the perfect power suit. *Science* **350**, 270–273 (2015).
8. L. N. Awad *et al.*, A soft robotic exosuit improves walking in patients after stroke. *Sci. Transl. Med.* **9**, eaai9084 (2017).
9. E. T. Roche *et al.*, Soft robotic sleeve supports heart function. *Sci. Transl. Med.* **9**, eaaf3925 (2017).
10. J. Folkman, A. Moscona, Role of cell shape in growth control, *Nature*. **273**, 345–349 (1978).
11. C. S. Chen, M. Mrksich, S. Huang, G. M. Whitesides, D. E. Ingber, Geometric control of cell life and death. *Science* **276**, 1425–8 (1997).
12. C. A. Cezar *et al.*, Biologic-free mechanically induced muscle regeneration. *Proc. Natl. Acad. Sci. U. S. A.* **113**, 1534–9 (2016).
13. C. P. Heisenberg, Y. Bellaïche, Forces in tissue morphogenesis and patterning. *Cell*. **153** (2013).
14. C. Huang, J. Holfeld, W. Schaden, D. Orgill, R. Ogawa, Mechanotherapy: Revisiting physical therapy and recruiting mechanobiology for a new era in medicine. *Trends Mol. Med.* **19**, 555–564 (2013).
15. J. G. McCarthy, E.J. Stelnicki, B. J. Mehrara, M. T. Longlaker, Distraction osteogenesis of the craniofacial skeleton. *Plast. Reconstr. Surg.* **107**, 1812-1827 (2001).
16. A. Bozkurt *et al.*, Retrospective analysis of tissue expansion in reconstructive burn surgery: evaluation of complication rates. **34** 1113-1118 (2008).
17. L. Lancerotto, D. P. Orgill, Mechanoregulation of Angiogenesis in Wound Healing. *Adv. wound care*. **3**, 626–634 (2014).
18. E. C. Novosel, C. Kleinhans, P. J. Kluger, Vascularization is the key challenge in tissue engineering. *Adv. Drug Deliv. Rev.* **63**, 300–311 (2011).

19. A. S. Mao, D. J. Mooney, Regenerative medicine: Current therapies and future directions. *Proc. Natl. Acad. Sci. U. S. A.* **112**, 14452–9 (2015).
20. A. Atala, F. K. Kasper, A. G. Mikos, Engineering complex tissues. *Sci. Transl. Med.* **4**, 160rv12 (2012).
21. J. E. Foker, T. C. Kendall Krosch, K. Catton, F. Munro, K. M. Khan, Long-gap esophageal atresia treated by growth induction: the biological potential and early follow-up results. *Semin. Pediatr. Surg.* **18**, 23–9 (2009).
22. H. Koga *et al.*, Distraction-induced intestinal enterogenesis: Preservation of intestinal function and lengthening after re-implantation into normal jejunum. *Ann. Surg.* **255**, 302–310 (2012).
23. H. B. Kim *et al.*, A novel treatment for the midaortic syndrome. *N. Engl. J. Med.* **367**, 2361–2 (2012).
24. D. D. Damian *et al.*, Robotic implant to apply tissue traction forces in the treatment of esophageal atresia. *Proc. - IEEE Int. Conf. Robot. Autom.*, 786–792 (2014).
25. P. F. M. Pinheiro, A. C. Simões e Silva, R. M. Pereira, Current knowledge on esophageal atresia. *World J. Gastroenterol.* **18**, 3662–72 (2012).
26. M. H. Ross, G. I. Kaye, W. Pawlina, *Histology: A Text and Atlas with Cell and Molecular Biology* (Lippincott Williams & Wilkins, 2002), pp. 476, 479-481. [fourth edition]
27. C. A. Powell, B. L. Smiley, J. Mills, H. H. Vandenburgh, Mechanical stimulation improves tissue-engineered human skeletal muscle. *Am. J. Physiol. Cell Physiol.* **283**, 1557-65 (2002).
28. B. S. Kim, J. Nikolovski, J. Bonadio, D. J. Mooney, Cyclic mechanical strain regulates the development of engineered smooth muscle tissue. *Nat Biotechnol*. 17, 979-83 (1999).
29. R. L. Mauck *et al.,* Functional tissue engineering of articular cartilage through dynamic loading of chondrocyte- seeded agarose gels. *J. Biomech. Eng.* **122**, 252–260 (2000).
30. L. E. Niklason *et al.*, Functional arteries grown in vitro. *Science* **284**, 489-493 (1999).
31. L. Xu *et al.*, 3D multifunctional integumentary membranes for spatiotemporal cardiac measurements and stimulation across the entire epicardium. *Nat. Commun.* **5**, 3329 (2014).
32. G. Z. Lum *et al.*, Shape-programmable magnetic soft matter. *Proc. Natl. Acad. Sci. U. S. A.* **113**, E6007–E6015 (2016).
33. S. H. Lee *et al.*, Implantable batteryless device for on-demand and pulsatile insulin administration. *Nat. Commun.* **8**, 15032 (2017).
34. J. Kim *et al.*, Battery-free, stretchable optoelectronic systems for wireless optical characterization of the skin. *Sci. Adv.* **2**, e1600418 (2016).
35. B. Lu *et al.*, Ultra-flexible Piezoelectric Devices Integrated with Heart to Harvest the Biomechanical Energy. *Sci. Rep.* **5**, 16065 (2015).

Acknowledgments:
Special thanks to Dr. Arthur Nedder, Naomi Crilley, Cara Pimental, Elizabeth Pollack, and Courtney White for their veterinary assistance.
Funding: Supported by Swiss National Science Foundation (P300P2_151248), Boston Children's Hospital Translational Research Program and Manton Center for Orphan Disease Research (Innovator Award).